

Carrier properties of Bi(111) grown on mica and Si(111)

Zijian Jiang, V. Soghomonian , and J. J. Heremans 

Physics Department, Virginia Tech, Blacksburg, Virginia 24061, USA

 (Received 25 May 2021; revised 14 August 2022; accepted 14 September 2022; published 23 September 2022)

A comparison is presented between properties of Bi(111) films grown by Stranski-Krastanov epitaxy on Si(111) 7×7 and by van der Waals epitaxy on mica substrates. Thin film morphologies and electronic transport properties of Bi(111) films of variable thickness are investigated for each growth method. Atomic force micrographs for Bi(111) films on mica reveal clearly defined triangular regions consisting of layered steps with height 0.4 nm, corresponding to the Bi(111) bilayer height. Variable-temperature electronic transport measurements show the existence of a quantum confinement-induced energy gap in the film interiors, resulting in a semimetal-to-semiconductor transition. Magnetotransport analysis in a three-carrier model including metallic electrons in surface states and electrons and holes in the films' interiors provides a detailed study of densities, mobilities, and mean-free paths of the three carrier types. Improved electronic transport properties are found in Bi(111) films of higher thickness on mica compared to on Si(111), a likely result of the largely strain-free van der Waals epitaxial growth.

DOI: [10.1103/PhysRevMaterials.6.095003](https://doi.org/10.1103/PhysRevMaterials.6.095003)

Bi and particularly Bi surfaces exhibit electronic properties that render them compelling platforms for quantum physics and spintronics studies. Bulk Bi in pure crystalline form is a semimetal, with low and equal electron and hole densities both $\sim 3 \times 10^{23} \text{ m}^{-3}$ for $T \lesssim 30 \text{ K}$ while higher but still equal electron and hole densities are observed at higher T , namely both up to $\sim 2.5 \times 10^{24} \text{ m}^{-3}$ at $T = 300 \text{ K}$ [1–3]. Pronounced Rashba-type spin-orbit interaction (SOI) exists in the surface electron states at Bi(111) surfaces [4–13]. The electronic properties of films and surfaces are sensitive to growth conditions, and to harness the notable quantum properties of Bi surfaces, efforts to grow high quality Bi thin films are a necessity. Such growth is challenging, the aim being to obtain Bi films with electronic properties, namely carrier density and mobility values, comparable to bulk in the film's interior and preserving the electronic properties of the surface states. Bi growth on various substrates such as Si(111) [8,14,15], SiO₂ [16,17] and others [4,7,18–21], have resulted in films with different morphologies, crystalline orientations, and properties. To date, reports indicate high quality Bi film growth on Si(111) [8,10,14,15,22–24]. In this paper, we compare the physical and electronic properties of Bi films grown on Si(111) and mica.

I. BI FILM GROWTH AND MORPHOLOGICAL PROPERTIES

Bi films of various thicknesses d were deposited on mica via van der Waals epitaxy (vdWE) [13] and on Si(111) substrates via Stranski-Krastanov epitaxy. Broadly, in Stranski-Krastanov epitaxial growth, the interaction between the substrate and epilayer is often covalent or ionic,

and film growth and characteristics are influenced by surface dangling bonds, surface states, surface preparation, and lattice mismatch [25,26]. Lattice mismatch results in pseudomorphic strained layers initially affecting overall film properties. In contrast, in vdWE the interaction is nonbonding and hence weak, allowing for largely strain-free film growth on substrates even in the presence of lattice mismatch [13,26–28]. vdWE is a choice when the substrate and/or the epilayer possess a van der Waals surface without dangling bonds, realized in 2D materials with naturally completely terminated surfaces, such as graphene and mica [29,30]. Epilayers of Sb, Ge, and Ge/Sb on mica have shown high crystalline quality [31,32], guiding the choice of mica for high quality Bi film growth. Even with considerable lattice-mismatch between the epitaxial Bi layer and the mica substrate (monoclinic, surface lattice constants $a_{\text{mica}} = 519 \text{ pm}$, $b_{\text{mica}} = 904 \text{ pm}$) [33], the weak interaction between the two allow for unstrained growth with a lattice constant of $a_{\text{Bi}(111)} = 454 \text{ pm}$, the bulk lattice constant of Bi in a plane normal to the trigonal (c axis) axis. Indeed when deposited on a freshly cleaved mica ab surface, the trigonal axis of Bi appears perpendicular to the mica surface, yielding a Bi(111) surface [using the rhombohedral Bi(111) notation vs the Bi(001) simplified hexagonal notation] [13]. On the other hand, the lattice mismatch between Bi(111) and Si(111) surface ($a_{\text{Si}(111)} = 384 \text{ pm}$) is compensated by the occurrence of magic mismatch between the Bi(111) phase and the Si(111) 7×7 surface, with a relation of $6|a_{\text{Bi}(111)}| = 7|a_{\text{Si}(111)}|$. The growth of the Bi(111) phase on the Si(111) 7×7 surface shows excellent azimuthal alignment after it is transformed from the lattice-mismatched Bi{012} phase [14].

Bi films with $d = 10, 20, 40,$ or 60 nm were deposited on mica by vdWE and on Si(111) 7×7 by Stranski-Krastanov epitaxy. To understand the evolution of electronic transport properties with d , additionally a Bi film with $d = 1000 \text{ nm}$ was deposited on mica by vdWE. For the vdWE, freshly

*heremans@vt.edu

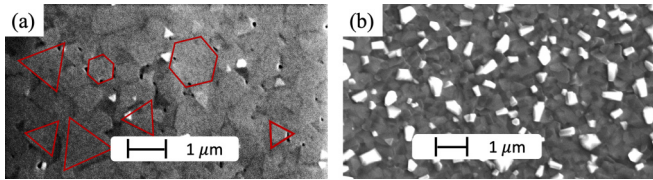


FIG. 1. Representative SEM micrograph of a 40 nm Bi(111) film (a) on mica and (b) on Si(111). In (a) red outlines delineate triangular and hexagonal growth patterns, which are not observed in (b). The patterns are consistent with the rhombohedral crystal structure of Bi(111) thin films.

cleaved mica substrates were preheated at 250 °C for at least 24 hr under ultrahigh vacuum in the growth chamber. High-purity (99.999%) Bi was deposited by thermal evaporation at a base pressure of 10^{-8} Torr on the mica held at 295 K. This substrate temperature was found to be within a range of temperatures yielding films optimized for large grain size and lower roughness. Deposition occurred through an aluminum shadowmask with apertures of diameters $\sim 500 \mu\text{m}$ placed on the mica *ab* surface. Bi films of varying d were deposited at a rate of $0.35 \text{ BL}_{111}/\text{min}$ ($0.14 \text{ nm}/\text{min}$), with one Bi bilayer = $1.0 \text{ BL}_{111} = 0.39 \text{ nm}$ [14,34]. The deposition rate and d were measured with less than 5% error by a quartz microbalance. To increase the grain size and decrease surface roughness, post growth the films were annealed at $95 \pm 5 \text{ }^\circ\text{C}$ for 1 hr at 10^{-8} Torr. For the Stranski-Krastanov epitaxy of Bi on Si(111) surfaces, thoroughly cleaned $4 \times 4 \text{ mm}$ pieces of Si(111) wafer were loaded into the growth chamber. The Si(111) 7×7 surface reconstruction was achieved by the following annealing treatment at 1×10^{-8} Torr. The substrate was outgassed at 600 °C for 5 hr to remove any oxide layer, followed by a 2-min flash heating where substrate temperature was raised to 1200 °C within a 3-min time duration. The sample was cooled slowly to room temperature to avoid $\sqrt{3} \times \sqrt{3}$ reconstruction [14,34,35]. Lastly, Bi was deposited onto the Si(111) 7×7 reconstructed surface, with the Si(111) substrate held at 295 K. As for the vdWE, this substrate temperature was found to lie within a range of temperatures yielding optimized films. The Bi deposition process, the growth rate and the post-growth annealing process were identical to the vdWE processes.

Bi(111) film morphologies were probed by scanning electron microscopy (SEM) and atomic force microscopy (AFM). In Fig. 1, we compare SEM micrographs of Bi films with $d = 40 \text{ nm}$, on mica [Fig. 1(a)] and Si(111) [Fig. 1(b)]. Bi films on mica [Fig. 1(a)] appear more uniform and with larger grain size, up to $\sim 1 \mu\text{m}$, than on Si(111). Moreover, Bi films on mica show characteristic triangular or hexagonal growth patterns [highlighted in red contours in Fig. 1(a)], confirming the rhombohedral crystal structure of Bi(111) thin films having their trigonal axis perpendicular to the mica surface. Bi films on Si(111) [Fig. 1(b)] present rougher surfaces and do not show the triangular or hexagonal growth patterns. In Fig. 2, we compare AFM micrographs of Bi films with $d = 10 \text{ nm}$ on mica [Fig. 2(a)], $d = 40 \text{ nm}$ on mica [Fig. 2(c)], $d = 10 \text{ nm}$ on Si(111) [Fig. 2(e)], and $d = 40 \text{ nm}$ on Si(111) [Fig. 2(g)]. Figure 2(a) ($d = 10 \text{ nm}$ on mica), Fig. 2(c) ($d = 40 \text{ nm}$ on mica), and Fig. 2(e) [$d = 10 \text{ nm}$ on Si(111)] exhibit a layered step surface with triangular terraces. Corresponding

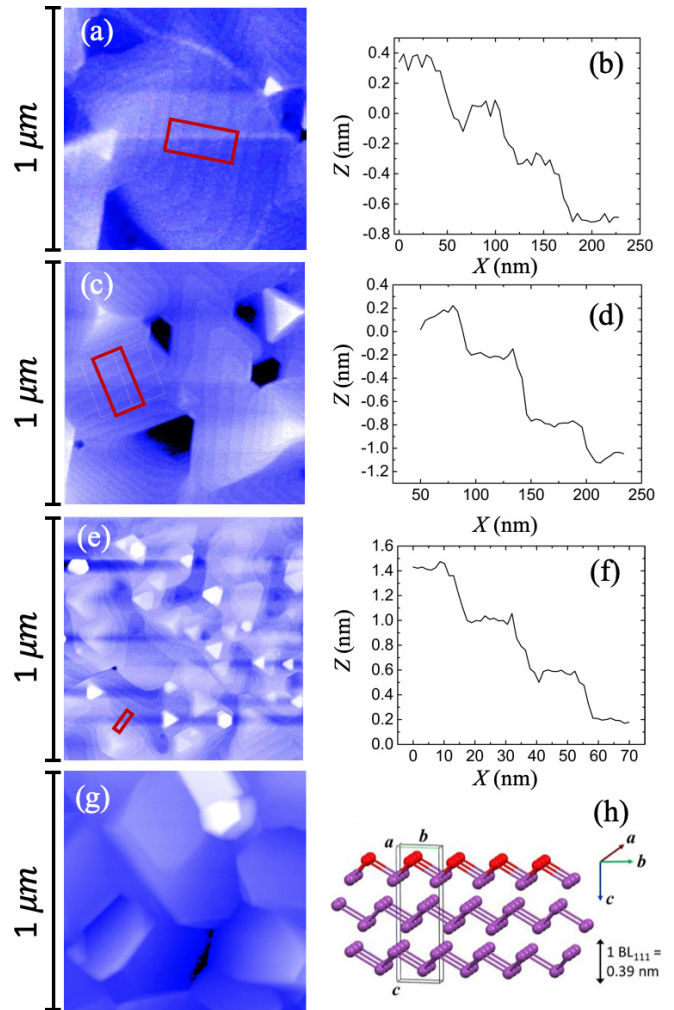


FIG. 2. (a) AFM micrograph of a $1 \mu\text{m} \times 1 \mu\text{m}$ area of a 10-nm Bi(111) film on mica, showing layered growth and triangular growth patterns. (b) Height profile (Z) vs horizontal distance (X) in the length direction of the red box in (a). (c) AFM micrograph of a $1 \mu\text{m} \times 1 \mu\text{m}$ area of a 40-nm Bi(111) film on mica, showing layered growth and triangular growth patterns. (d) Height profile (Z) vs horizontal distance (X) in the length direction of the red box in (c). (e) AFM micrograph of a $1 \mu\text{m} \times 1 \mu\text{m}$ area of a 10-nm Bi(111) film on Si(111), showing layered growth and triangular growth patterns. (f) Height profile (Z) vs horizontal distance (X) in the length direction of the red box in (e). (g) AFM micrograph of a $1 \mu\text{m} \times 1 \mu\text{m}$ area of a 40-nm Bi(111) film on Si(111) where no triangular growth patterns or terraces are observed. (h) Schematic of the Bi(111) bilayer structure, with surface atoms indicated in red, along with the BL_{111} spacing, the unit cell, and the trigonal c axis indicated.

height profiles Z vs lateral distance X obtained are depicted in Figs. 2(b), 2(d), and 2(f). From the profiles the step heights between adjacent terraces are measured to be $0.39 \pm 0.02 \text{ nm}$ corresponding to 1.0 BL_{111} [13,14,34], again confirming that we obtained Bi(111) surfaces. Figure 2(h) shows a schematic of the Bi(111) bilayer structure, with surface atoms indicated in red, along with the BL_{111} spacing, the unit cell, and the trigonal c axis. We note that layered triangular terraces are observed for both $d = 10 \text{ nm}$ and 40 nm on mica, while Fig. 2(g) for $d = 40 \text{ nm}$ on Si(111) shows irregular grains and lacks

a layered surface. Layered triangular terraces are observed only for the thinner 10 nm Bi films on Si(111). Measuring the root-mean-square roughness (R_q) obtained via AFM, we find that for $d = 10$ nm on mica we have $R_q = 2.3$ nm; for $d = 40$ nm on mica we have $R_q = 1.5$ nm; for $d = 10$ nm on Si(111) we have $R_q = 1.6$ nm; and for $d = 40$ nm on Si(111) we have $R_q = 9.3$ nm. From the lack of stepped terraces and the increased R_q we deduce that the Bi film with $d = 40$ nm on Si(111) has a lesser crystalline and surface quality and that higher quality Bi(111) films on Si(111) may have to be restricted to lower $d \lesssim 10$ nm. A comparison between Figs. 2(a) and 2(c) (10 nm and 40 nm on mica) and Fig. 2(e) [10 nm on Si(111)] further shows that growth on mica leads to larger grain sizes than on Si(111).

The respective morphologies obtained on mica and Si(111) depend on several factors, possibly necessitating differing optimization strategies only a subset of which were explored here for Bi(111). While the weakly interacting substrate in vdWE can lead to strain-free film growth, it can also result in 3D growth, yielding islands of varying heights rather than smoother 2D growth. The growth on Si(111) on the other hand can initiate with a wetting layer that mitigates the strain between film and substrate. In this paper focusing on electronic transport properties, the competing advantages result in comparable yet different electronic transport properties for the different substrates as function of d , as discussed below.

II. ELECTRONIC AND MAGNETOTRANSPORT PROPERTIES

A. Transport parameters of interior electron and holes and surface electrons

Magnetotransport measurements were performed in magnetic field B applied normal to the Bi(111) surface, as function of d and of measurement temperature T over the range 4.1 K–296 K, on samples in the van der Pauw configuration. Electronic conduction through Bi(111) films occurs both through the interior of the film and through surface states, leading to a 3-carrier model as explained below. The interior of the films host two carrier types, electrons and holes, with electron (hole) mobilities we denote μ (ν) and 3-dimensional electron (hole) densities we denote n (p). The interior of the films hence contributes an interior or bulk 3-dimensional conductivity $\sigma_b = ne\mu + p\nu$, with e the electron charge. At the Bi(111) surface metallic surface states of high conductivity exist [4–13,19]. We assume that transport properties of the Bi(111) surface states are dominated by higher-conductivity surface electrons, with mobility μ_s and areal density N_s . The surface states then contribute a 2-dimensional conductivity $\sigma_{s\Box} = N_s e \mu_s$ ($\sigma_{s\Box}$ in units of Ω^{-1} is the inverse sheet resistance of the surface states). We neglect the contributions from lower-conductivity surface holes [4,6,10,13], which also reduces the proliferation of parameters in the multicarrier model. We hence use a 3-carrier model [19]. The overall 3-dimensional conductivity σ of the films is then found as the sum of interior and surface terms, $\sigma = \sigma_b + \frac{\sigma_{s\Box}}{d}$. The measurements at $B = 0$ in fact deliver an overall film sheet resistance (overall 2-dimensional resistivity in units of Ω/\Box) $R_{\Box} = \rho/d$, from which we obtain ρ as the

TABLE I. Bi film sheet resistance R_{\Box} and resistivity ρ at $T = 4.1$ K and 296 K on mica for $d = 10, 20, 40, 60, 1000$ nm and on Si(111) for $d = 10, 20, 40, 60$ nm ($B = 0$).

| mica | 10 nm | 20 nm | 40 nm | 60 nm | 1000 nm |
|--------------------------------------|-------|-------|-------|-------|---------|
| R_{\Box} (4.1 K, Ω/\Box) | 127 | 159 | 94.3 | 28.5 | 0.967 |
| ρ (4.1 K, $\mu\Omega\text{m}$) | 1.27 | 3.17 | 3.77 | 1.71 | 0.967 |
| R_{\Box} (296 K, Ω/\Box) | 127 | 78.0 | 35.3 | 9.00 | 0.545 |
| ρ (296 K, $\mu\Omega\text{m}$) | 1.27 | 1.56 | 1.41 | 0.540 | 0.545 |
| Si(111) | 10 nm | 20 nm | 40 nm | 60 nm | |
| R_{\Box} (4.1 K, Ω/\Box) | 342 | 297 | 132 | 107 | |
| ρ (4.1 K, $\mu\Omega\text{m}$) | 3.42 | 5.94 | 5.29 | 6.41 | |
| R_{\Box} (296 K, Ω/\Box) | 352 | 140 | 35.3 | 13.6 | |
| ρ (296 K, $\mu\Omega\text{m}$) | 3.52 | 2.79 | 1.41 | 0.814 | |

overall 3-dimensional resistivity with $\rho = \rho(B = 0) = 1/\sigma$. Table I lists the values of R_{\Box} and ρ at $T = 4.1$ K and 296 K at $B = 0$ for Bi on mica and on Si(111). The measurements at $B \neq 0$ yield longitudinal magnetoresistivity $\rho(B)$ and Hall (transverse) resistance $R_H(B)$ from which the mobilities and densities of the multiple carriers are deduced via multicarrier magnetotransport analysis.

B. Quantum confinement effects, phonon scattering, and model for $\rho(T)$

Bulk Bi is a semimetal and displays metallic behavior in $\rho(T)$ wherein $\rho(T)$ decreases monotonically as T decreases [1–3]. But more complex behavior in $\rho(T)$ is typically observed due to quantum confinement effects in the interior of Bi thin films when d is comparable to the Fermi wavelength λ_F , which in Bi is long due to low carrier densities ($\lambda_F \approx 30$ nm). The quantum confinement phenomena affect $\sigma_b(T)$. Due to the dependence on T of $\sigma_b(T)$, when d is small $\rho(T)$ can exhibit a semimetal-to-semiconductor transition (SMSCT) at a transition temperature T_C , with metallic behavior for $T < T_C$ and semiconducting behavior for $T > T_C$ wherein $\rho(T)$ increases as T decreases [6–9,19,36,37]. Quantum confinement is predicted to open an energy gap $\Delta E \approx 15$ meV to 100 meV, depending on d , T , and λ_F , in the interior of a Bi film [7–9,19,36–39]. In the interior of the film carrier density is then governed by thermal activation across ΔE , yielding the semiconducting behavior observed for $T > T_C$. The upper limit of d for which the SMSCT in Bi films can be observed depends on precise film properties and has been variously estimated at 23 nm... 90 nm [7,37–39]. The experimental search for the SMSCT has been complicated by the existence of the metallic surface states [4–13,19]. Reference [7] derives $\sigma(T)$ at $B = 0$ from expressions for interior σ_b , surface $\sigma_{s\Box}$, and their sum,

$$\begin{aligned} \sigma_b(T) &= \alpha e^{-\Delta E/(2k_B T)} \\ \sigma_{s\Box}(T) &= \frac{1}{(R_{rs\Box} + sT)} \\ \Rightarrow \sigma(T) &= \alpha e^{-\Delta E/(2k_B T)} + \frac{1}{d(R_{rs\Box} + sT)}. \end{aligned} \quad (1)$$

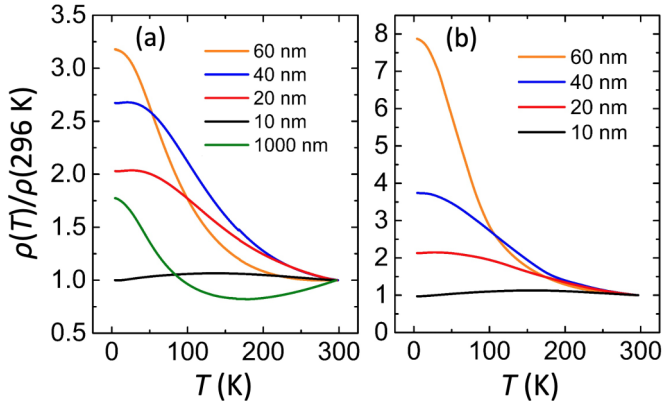


FIG. 3. Normalized $\rho(T)/\rho(296\text{ K})$ at $B = 0$, vs T for $4.1\text{ K} \leq T \leq 296\text{ K}$ for Bi(111) films (a) on mica with $d = 10, 20, 40, 60$, and 1000 nm , and (b) on Si(111) with $d = 10, 20, 40$, and 60 nm . A SMSCT is observed at $T = T_C$, with T_C largely independent of substrate.

The first expression describes the semiconducting behavior of the interior $\sigma_b(T)$ due to energy gap ΔE , where α is a prefactor with units of 3-dimensional conductivity and k_B is the Boltzmann constant. The second expression, for the surface $\sigma_{s\Box}(T)$, is appropriate for a 2D metal [7]. It describes that the metallic behavior of $\sigma_{s\Box}(T)$ originates in a T -independent residual sheet resistance $R_{rs\Box}$ due to Coulombic impurity scattering, and T -dependent sheet resistance due to electron-phonon scattering, written as sT with s a phonon scattering parameter having units Ω/K .

Reference [7] quantifies $\Delta E \propto 1/d^2$, expressing the quantum confinement effect, whereas we will allow a more general $\Delta E \propto 1/d^p$ behavior ($p > 0$). As d and T increase, σ_b increases while $\sigma_{s\Box}$ decreases, leading to complicated behavior of $\rho(T, d) = 1/\sigma(T, d)$. For lower d (larger ΔE), Eq. (1) can lead to $\rho(T)$ showing the SMSCT with $\rho(T)$ increasing with decreasing T for $T > T_C$ and $\rho(T)$ decreasing with decreasing T for $T < T_C$, showing a maximum in $\rho(T)$ vs T . Yet for higher d (smaller ΔE), Eq. (1) can lead to $\rho(T)$ showing an inverse SMSCT with $\rho(T)$ decreasing with decreasing T for $T > T_C$ and $\rho(T)$ increasing with decreasing T for $T < T_C$, showing a minimum in $\rho(T)$ vs T . As shown in Fig. 3, we have experimentally observed both maxima and minima in $\rho(T)$ vs T in Bi(111) on mica and/or Si(111) depending on d , in accordance with Eq. (1).

C. Results at $B = 0$: $\rho(T)$, T_C , s , ΔE

Figure 3 depicts the normalized $\rho(T)/\rho(296\text{ K})$ ($B = 0$) for various d on mica and Si(111). As predicted by Eq. (1), a SMSCT with maximum at T_C is observed for lower d . The maximum in $\rho(T)$ is visible in Fig. 3 for $d = 10, 20$, and 40 nm on mica, and for $d = 10$ and 20 nm on Si(111). For $d = 60\text{ nm}$ on mica and $d = 40$ and 60 nm on Si(111) we have $T_C < 4.1\text{ K}$, which falls below the measurement temperatures. A SMSCT with minimum is observed for the higher $d = 1000\text{ nm}$ (deposited on mica only). The dependence of T_C on d is shown in Fig. 4 (filled symbols, left axis) for both mica and Si(111) substrates, showing that thinner films yield higher T_C . For $T_C < 4.1\text{ K}$ [$d = 60\text{ nm}$ on mica and $d = 40$

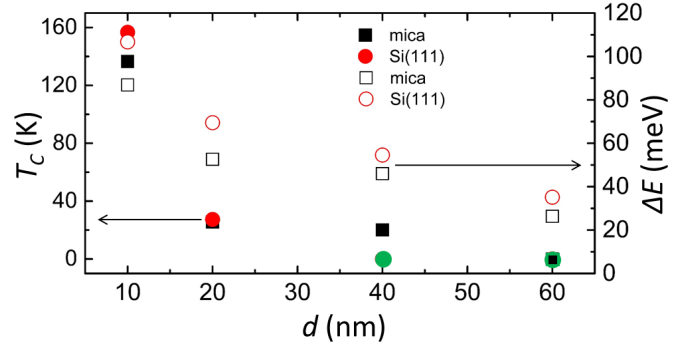


FIG. 4. Left axis, filled symbols: Dependence of T_C on film thickness d for Bi(111) on mica and on Si(111). Green datapoints denote $T_C < 4.1\text{ K}$ (cfr text). Right axis, open symbols: Dependence of ΔE on film thickness d for Bi(111) on mica and on Si(111).

and 60 nm on Si(111)] Fig. 4 uses green symbols at $T_C \rightarrow 0$ to complete the graph. The increase in T_C with decreasing d is also observed in the literature [7,9], and is in accordance with Eq. (1).

We have performed numerical fits of $\rho(T)$ to Eq. (1) for $d = 10, 20, 40$, and 60 nm on mica and Si(111) to extract the values of s and ΔE , and found that Eq. (1) reflects the data quite well. We find small values for s , maximally $0.5\text{ }\Omega/\text{K}$ and averaging $\sim 0.1\text{ }\Omega/\text{K}$. This indicates that not only electron-phonon scattering but also Coulombic impurity scattering, which determines the residual $R_{rs\Box}$, is important in the Bi(111) surface states, as expected for a surface electron system exposed to atmosphere.

The values of ΔE are plotted vs d in Fig. 4 (open symbols, right axis) for both mica and Si(111). The values $26\text{ meV} \leq \Delta E \leq 106\text{ meV}$ fall within the expected range [7–9,19,36–39] and as predicted, lower d yields higher ΔE . However while quantum confinement in the simplest approximation would yield $\Delta E \propto 1/d^2$ [7], we find $\Delta E \propto 1/d^p$ with $p \approx 0.56 \pm 0.09$. The reason for the milder dependence on d than predicted for quantum confinement is presently undetermined, and $p \approx 0.56 \pm 0.09$ is presented as an experimental finding. While we observe no influence of the substrate on the presence of the SMSCT, Fig. 4 (open symbols, right axis) shows that ΔE is at all d larger for Bi(111) on Si(111) than on mica.

D. Effects of film roughness

Since d denotes the average thickness, the film roughness described by R_q will affect the averaging over sample area of quantities nonlinear in d , here specifically $\Delta E \propto 1/d^p$. Calculations were performed for the area-averaged ΔE that would result assuming a simplified sinusoidal roughness landscape, $d_r(\vec{r}) = d + \sqrt{2}R_q \sin(2\pi|\vec{r}|/s)$, where s stands for the average lateral size of the grains and as above d is the average thickness as reported by the quartz microbalance. It is found that roughness will lead to an effectively higher ΔE , as if corresponding to an effective thickness $< d$, independent of s if averaged over large areas. The effect ranges from 17% higher ΔE for the 40-nm film on Si(111) (with high R_q/d) to 0.1% higher for the 40-nm film on mica (with low R_q/d). The values ΔE are determined by numerical fits of $\rho(T)$ to Eq. (1) however, and hence the sole effect of roughness on ΔE

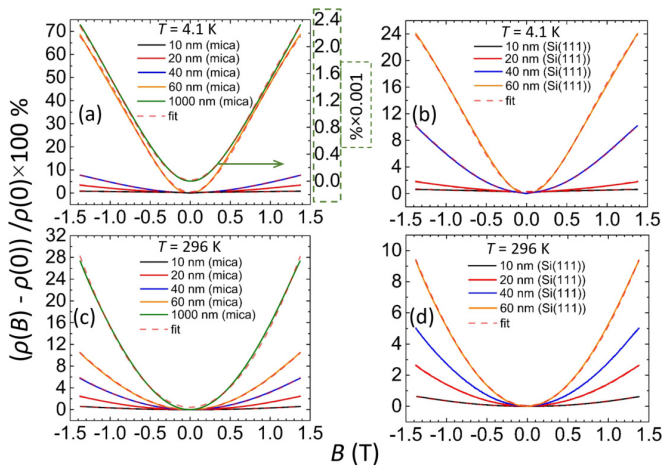


FIG. 5. Magnetoresistivity vs B over $-1.4\text{ T} < B < 1.4\text{ T}$ for Bi(111) films, plotted as $(\rho(B) - \rho(B=0))/\rho(B=0)$, with $d = 10, 20, 40, 60,$ and 1000 nm on mica and $d = 10, 20, 40,$ and 60 nm on Si(111), (a) at $T = 4.1\text{ K}$ on mica, (b) at $T = 4.1\text{ K}$ on Si(111), (c) at $T = 296\text{ K}$ on mica, and (d) at $T = 296\text{ K}$ on Si(111). For $d = 1000\text{ nm}$ in (a) the magnetoresistivity scale is scaled by a factor 0.001. Fits to the 3-carrier model are plotted as dashed lines (same color for all d).

is a rescaling of the d axis in Fig. 4 to an effective thickness $< d$. Since the effect is not large, Fig. 4 was not modified to reflect this effective thickness. Further, unrealistically high values of relative roughness R_q/d are necessary to increase the low exponent $p \approx 0.56$ to a value ≈ 2 . While roughness can contribute to a slight lowering of the experimentally deduced p , the effectively observed value of $p \approx 0.56$ cannot fully be explained from roughness. The effect of roughness can however contribute to the observation in Fig. 4 of higher ΔE for films on Si(111) than on mica, given the overall higher R_q/d on Si(111).

E. Magnetotransport results: Magnetoresistivity $\rho(B)$ and Hall resistance $R_H(B)$

In Figs. 5(a)–5(d), we compare $(\rho(B) - \rho(B=0))/\rho(B=0)$ vs B for various d on mica and Si(111), at $T = 4.1\text{ K}$ and 296 K . The normalized $\rho(B)$ facilitates comparison across d since the $\rho(B=0)$ differ by over an order of magnitude across d . Figures 6(a)–6(d) compare $R_H(B)$ vs B for various d on mica and Si(111), at $T = 4.1\text{ K}$ and 296 K , plotted such that a positive slope of $R_H(B)$ vs B denotes prevalence of hole transport in the Hall effect (dependent on n, p, N_s as well as $\mu, \nu,$ and μ_s). We attribute the near-quadratic $\rho(B)$ in Fig. 5 and the nonlinear $R_H(B)$ in Fig. 6 to the presence of multiple carriers [13,19,37], leading to the use of the 3-carrier model. While quantitative results for $n, p, N_s, \mu, \nu,$ and μ_s from the 3-carrier model are discussed below, inspection of Figs. 5(a)–5(d) and Figs. 6(a)–6(d) already reveals trends. Figures 5(a)–5(d) show that higher $(\rho(B) - \rho(B=0))/\rho(B=0)$ are obtained at larger d . At $T = 4.1\text{ K}$, $(\rho(B) - \rho(B=0))/\rho(B=0)$ is noticeably larger for $d = 60\text{ nm}$ and 1000 nm on mica [Fig. 5(a)] and for $d = 60\text{ nm}$ on Si(111) [Fig. 5(b)] than in the thinner films. At $B = 1.4\text{ T}$, $(\rho(B) - \rho(B=0))/\rho(B=0)$ reaches up to

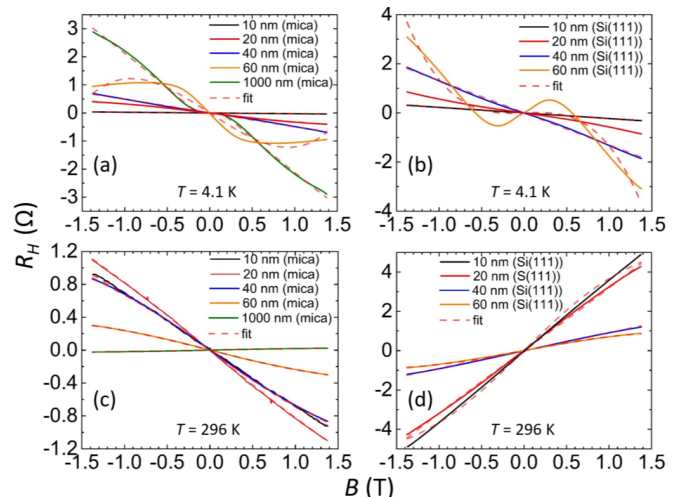


FIG. 6. Hall resistance $R_H(B)$ vs B over $-1.4\text{ T} < B < 1.4\text{ T}$ for Bi(111) films, with $d = 10, 20, 40, 60,$ and 1000 nm on mica and $d = 10, 20, 40,$ and 60 nm on Si(111), (a) at $T = 4.1\text{ K}$ on mica, (b) at $T = 4.1\text{ K}$ on Si(111), (c) at $T = 296\text{ K}$ on mica, and (d) at $T = 296\text{ K}$ on Si(111). Fits to the 3-carrier model are plotted as dashed lines (same color for all d).

2350% for $d = 1000\text{ nm}$ on mica (large magnetoresistivities in thicker Bi films were observed previously [40]). For a given d , Bi(111) on mica exhibits larger magnetoresistivities than on Si(111), particularly for larger d . Concomitantly Figs. 6(a) and 6(b) reveal stronger nonlinearity in $R_H(B)$ at $T = 4.1\text{ K}$ for $d = 60\text{ nm}$ and 1000 nm on mica and for $d = 60\text{ nm}$ on Si(111) than in the thinner films, pointing to the common multicarrier origin of both the near-quadratic $\rho(B)$ and the nonlinear $R_H(B)$. Inspection of the slope of $R_H(B)$ vs B in Figs. 6(a)–6(d) indicates a prevalent electron transport in the Hall effect in films with $d = 10, 20,$ and 40 nm on mica at both $T = 4.1\text{ K}$ and 296 K and on Si(111) at $T = 4.1\text{ K}$, while pointing to prevalent hole transport on Si(111) at $T = 296\text{ K}$ (this latter effect is attributable to $\nu > \mu$ in these samples, as discussed below). The prevalent electron transport in the Hall effect reflects the dominance of the Bi(111) electron surface states over the interior of the film for smaller d . Comparing Figs. 5(c) and 5(d) with Figs. 5(a) and 5(b), we find that for films on both mica and Si(111) at the higher $T = 296\text{ K}$ ($>T_C$ for all films), $(\rho(B) - \rho(B=0))/\rho(B=0)$ is comparatively reduced, particularly for larger d .

F. Carrier densities n, p, N_s , mobilities μ, ν, μ_s , mean-free paths, and effects of quantum confinement, bandstructure, and unintentional doping

Fitting approach. While the conventional 3-carrier model does not consider possible anisotropy of $\mu, \nu,$ and μ_s in Bi(111), the finite crystal grain size in the films will mitigate the effects of anisotropy. Accordingly, the model with 3 isotropic carrier bands provides a good description of the data and leads to credible values for $n, p, N_s, \mu, \nu,$ and μ_s , consistent with the literature, as discussed below. Preliminary fits to the 3-carrier model showed that for the Bi(111) surface states N_s does not vary significantly with d and T , and that μ_s does not vary significantly with d . However, μ_s decreases with

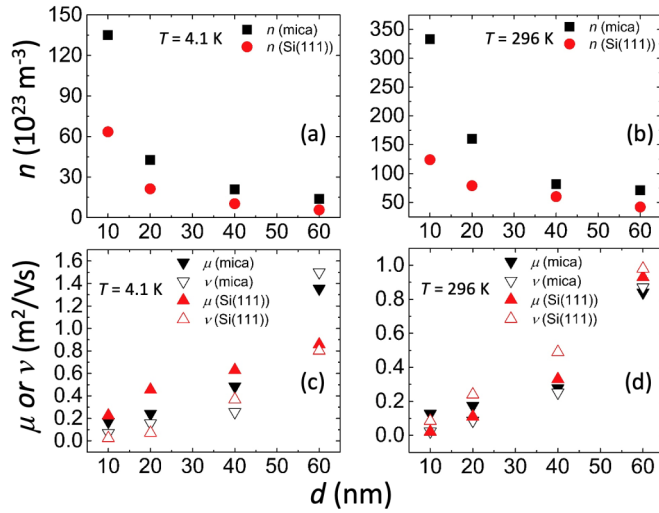


FIG. 7. Carrier densities $n = p$ and mobilities μ and ν vs d , extracted from 3-carrier model fits to the magnetoresistivity and Hall resistance, for Bi(111) films with $d = 10, 20, 40,$ and 60 nm on mica and Si(111). (a) $n = p$ at $T = 4.1$ K, (b) $n = p$ at $T = 296$ K, (c) μ and ν at $T = 4.1$ K, and (d) μ and ν at $T = 296$ K.

increasing T , attributed to increased phonon scattering at higher T . To reduce the fitting uncertainty due to the large number of fitting parameters, we fixed the values for the Bi(111) surface states in the fitting procedure, at $N_s = 3.25 \times 10^{15} \text{ m}^{-2}$ for $T = 4.1$ K and $T = 296$ K for all d , and at $\mu = 1.0 \text{ m}^2/\text{Vs}$ for $T = 4.1$ K and $\mu = 0.87 \text{ m}^2/\text{Vs}$ for $T = 296$ K for all d . Those values are comparable to values from previous studies [13]. Preliminary fitting also showed that for the interior of the Bi films $n \approx p$ holds at $T = 4.1$ K and $T = 296$ K for $d = 10, 20, 40,$ and 60 nm on mica and Si(111), but not for $d = 1000$ nm on mica. For $d = 10, 20, 40,$ and 60 nm at $T = 4.1$ K and $T = 296$ K, we hence used $n = p$. For these d the values of $n = p$ are graphed vs d in Figs. 7(a) and 7(b), and μ and ν are graphed vs d in Figs. 7(c) and 7(d).

Carriers in the $d = 1000$ nm film. For $d = 1000$ nm on mica we find at $T = 4.1$ K that $n = 2.82 \times 10^{23} \text{ m}^{-3}$, $p = 4.87 \times 10^{23} \text{ m}^{-3}$, $\mu = 22.1 \text{ m}^2/\text{Vs}$ and $\nu = 10.7 \text{ m}^2/\text{Vs}$, and at $T = 296$ K that $n = 3.75 \times 10^{24} \text{ m}^{-3}$, $p = 4.38 \times 10^{24} \text{ m}^{-3}$, $\mu = 0.89 \text{ m}^2/\text{Vs}$, and $\nu = 0.60 \text{ m}^2/\text{Vs}$. The values we obtain for $d = 1000$ nm on mica at $T = 296$ K are similar to values obtained on bulk polycrystalline samples in Ref. [41] where at $T = 300$ K it was found that $n = p \approx 3.69 \times 10^{24} \text{ m}^{-3}$, $\mu = 0.89 \text{ m}^2/\text{Vs}$, and $\nu = 0.60 \text{ m}^2/\text{Vs}$. Compared to our values for $d = 1000$ nm on mica, high-purity bulk single-crystals [1–3] yield comparable $n = p$ ($\sim 3 \times 10^{23} \text{ m}^{-3}$ for $T \lesssim 30$ K, $\sim 2.5 \times 10^{24} \text{ m}^{-3}$ for $T \approx 300$ K), and comparable μ and ν at $T \approx 300$ K ($\sim 0.60 \text{ m}^2/\text{Vs}$), but substantially higher μ and ν at $T \approx 4$ K ($\sim 500 - 2500 \text{ m}^2/\text{Vs}$). The similarity between mobilities at $T \approx 300$ K obtained on our film with $d = 1000$ nm on mica and on polycrystalline bulk material and on single-crystal bulk crystals can be understood from the dominance at higher T of phonon scattering and possibly intervalley scattering [2] (both diminishing the importance of scattering by defects). Also, for the film with $d = 1000$ nm a similarity to bulk properties can be expected because the contribution to the conductivity from the electron and holes in

the film interior dominates over the contribution of the surface electrons. We can estimate the mean-free path λ_n for electrons and λ_p for holes in the interior of the film with $d = 1000$ nm, assuming an approximately parabolic dispersion, and using 3 ellipsoidal Fermi surface pockets for electrons and a single Fermi surface pocket for holes. At $T = 4.1$ K the estimate yields $\lambda_n \approx \lambda_p \approx 1.8 \mu\text{m}$. Noting that at $T = 4.1$ K (where phonon and intervalley scattering are low) both λ_n and λ_p are similar to the film grain size, we surmise that at low T both μ and ν are in our thicker 1000-nm film limited by the finite grain size. On the other hand the values $\mu = 0.89 \text{ m}^2/\text{Vs}$ and $\nu = 0.60 \text{ m}^2/\text{Vs}$ at $T = 296$ K are limited by phonon scattering and possibly intervalley scattering. In the 1000 nm film at $T = 296$ K both λ_n and λ_p are estimated at $0.2 \mu\text{m}$.

Effects on n and p of quantum confinement, bandstructure and unintentional doping. Figures 7(a) and 7(b) contain $n = p$ graphed vs d for $d = 10, 20, 40,$ and 60 nm on mica and Si(111), and show that at both $T = 4.1$ K and 296 K $n = p$ increases as d decreases. Figures 7(a) and 7(b) also show that $n = p$ increases with increasing T , between 4.1 K and 296 K. The increase of $n = p$ with T in Bi films can be understood from two contributions. A first contribution originates from the existence of the quantum confinement energy gap ΔE (Fig. 4) in the interior of the film [7–9,19,36–39]. However, the increase of $n = p$ with T is also observed in high-purity bulk single-crystals where $\Delta E \rightarrow 0$ [1]. The increase of $n = p$ with T is in the literature [42,43] attributed to the small energy overlap E_0 (38 meV at 4 K) between the L-point electron band and the T-point hole band and the small bandgap E_g (13.6 meV at 4 K) separating the L-point electron band from lower bands. E_0 and E_g show strong dependencies on T and the small E_g allows thermal carrier excitation. The effects of E_0 and E_g bring the second contribution to our observed increase of $n = p$ with T in Bi films. Further, the increase in $n = p$ as d decreases indicates for both Bi films on mica and Si(111) an effective unintentional doping of the parts of the film closest to the substrate, possibly due to dislocations, offsetting the effect of quantum confinement (which will decrease $n = p$ with decreasing d due to larger ΔE). A substrate-dependent unintentional doping is also supported by the observation from Figs. 7(a) and 7(b) that $n = p$ on mica is higher than on Si(111). From Figs. 7(a) and 7(b) it is seen that $n = p$ increases by a factor ≈ 3 from $T = 4.1$ K to 296 K. On the other hand, the literature indicates that in high-purity bulk single crystals $n = p$ increases by a larger factor ≈ 8 from $T = 4$ K to 300 K [1], and over that same range of T , n and p increase by again a larger factor ≈ 11 in the thick film with $d = 1000$ nm on mica. It is thus apparent that in thin Bi films the dependence of $n = p$ on T is lessened compared to bulk crystals or thick films, possibly because the substrate-dependent unintentional doping mitigates both the quantum confinement effect (ΔE) and the bandstructural effects of E_0 and E_g . The dependence of $n = p$ on d and T in Bi(111) thin films hence hinges on a competition between the unintentional doping, quantum confinement, and bandstructural effects. We surmise that this competition contributes to the deviation we observe from the behavior $\Delta E \propto 1/d^2$ expected from pure quantum confinement [7], to the effectively observed behavior $\Delta E \propto 1/d^{0.56}$.

Discussion of μ and ν for $d = 10, 20, 40,$ and 60 nm. Figures 7(c) and 7(d) contain μ and ν graphed vs d for $d = 10, 20, 40,$ and 60 nm on mica and Si(111), and show that μ and ν decrease as d decreases, at both $T = 4.1$ K and 296 K, and show that μ and ν decrease with increasing T . The decrease in μ and ν with decreasing d can be attributed to the unintentional doping of the substrate introducing increased charged-impurity scattering in the parts of the film closest to the substrate, which have increased relative importance for thinner films. The decrease in μ and ν with increasing T is attributed to increased and dominant phonon and intervalley scattering at higher T [1–3]. At $T = 296$ K the values for μ and ν for the films with $d = 60$ nm on both mica and Si(111), ranging $0.84 - 0.98$ m²/Vs, closely resemble values obtained on the film with $d = 1000$ nm on mica (cfr above, $\mu = 0.89$ m²/Vs and $\nu = 0.60$ m²/Vs). Hence the dopant scattering induced by the substrate is already secondary to phonon and intervalley scattering at $T = 296$ K for d as low as 60 nm. At $T = 296$ K, Fig. 7(d) shows that for films on Si(111) we have $\nu > \mu$, which explains the observed prevalent hole transport in Fig. 6(d) as mentioned above. For $d = 60$ nm we also observe that at $T = 4.1$ K (where phonon and intervalley scattering are mitigated), μ and ν on mica substantially exceed μ and ν on Si(111) [1.43 m²/Vs on mica compared to ≈ 0.83 m²/Vs on Si(111)]. On the other hand for thinner films ($d < 60$ nm), at $T = 4.1$ K, Fig. 7(c) shows similar values for μ and ν for films on mica and Si(111).

Correlation with film morphology. The discussion of Fig. 2 similarly concluded that Bi(111) films on Si(111) of morphological quality comparable to Bi(111) on mica will only occur for lower d . The superior surface quality and electronic transport properties of the thicker ($d \sim 40$ – 60 nm) films on mica possibly result from the largely strain-free van der Waals epitaxial growth on mica bearing its fullest advantage at higher film thicknesses. The thinnest 10-nm Bi(111) films on Si(111) in fact show comparable surface characteristics from AFM analysis and comparable transport properties to 10-nm Bi(111) films on mica. An estimate of the mean-free path for the surface states (with N_s and μ_s quoted above) indicates 94 nm at $T = 4.1$ K and 82 nm at $T = 296$ K. For the carriers in the film interior, for $d = 60$ nm we estimate $\lambda_n, \lambda_p \approx 250$ nm, and for $d = 10, 20,$ and 40 nm we estimate $\lambda_n, \lambda_p \lesssim 80$ nm, for both $T = 4.1$ K and 296 K. Hence grain

sizes do not limit μ, ν or μ_s for Bi(111) films with $d = 10, 20, 40,$ or 60 nm. We finally note that in Figs. 7(a)–7(d) our values for n and p at $T = 4.1$ K are comparable to values measured at 5 K for similar d deposited on Si/SiO₂ in Ref. [19], whereas our values for μ and ν are substantially higher than values measured in Ref. [19].

III. CONCLUSIONS

In conclusion, we present a comparison of the electronic transport properties of Bi(111) films grown on mica and on Si(111). Included is an analysis of the electronic transport properties at 4.1 K and 296 K, in a 3-carrier model accounting for electrons in surface states and both electrons and holes in the film interiors. Bi films of thicknesses 10 nm, 20 nm, 40 nm, 60 nm, and 1000 nm were studied. AFM and SEM micrographs indicate that for Bi(111) film thickness above 10 nm, Bi(111) on mica has higher surface quality, with clearer triangular structured islands and lower roughness, than Bi(111) on Si(111). For Bi(111) films on mica, AFM reveals layered steps corresponding to the Bi(111) bilayer height. Temperature-dependent electronic transport measurements show the existence of a quantum confinement-induced energy gap in the film interiors of magnitude 26 meV to 106 meV depending on film thickness, leading to a semimetal-to-semiconductor transition in the film interior while the surface states remain metallic. Using magnetotransport measurements and a 3-carrier conduction model a detailed analysis is performed of the densities, mobilities and mean-free paths of the surface electrons and interior electrons and holes, and the values are compared with Bi film and single-crystal literature. Bi(111) films of higher thickness on mica show electronic transport properties superior to films on Si(111). The studies provide a method for obtaining high quality Bi(111) films on mica by van der Waals epitaxy, with potential for new Bi quantum and spintronics devices.

ACKNOWLEDGMENTS

The work was supported by the U.S. Department of Energy, Office of Basic Energy Sciences, Division of Materials Sciences and Engineering under award DOE DE-FG02-08ER46532.

-
- [1] J. P. Michenaud and J. P. Issi, Electron and hole transport in bismuth, *J. Phys. C* **5**, 3061 (1972).
 - [2] R. Hartman, Temperature dependence of the low-field galvanomagnetic coefficients of bismuth, *Phys. Rev.* **181**, 1070 (1969).
 - [3] R. N. Zitter, Small-field galvanomagnetic tensor of bismuth at 4.2° K, *Phys. Rev.* **127**, 1471 (1962).
 - [4] Y. M. Koroteev, G. Bihlmayer, J. E. Gayone, E. V. Chulkov, S. Blügel, P. M. Echenique, and P. Hofmann, Strong Spin-Orbit Splitting on Bi Surfaces, *Phys. Rev. Lett.* **93**, 046403 (2004).
 - [5] C. R. Ast, J. Henk, A. Ernst, L. Moreschini, M. C. Falub, D. Pacilé, P. Bruno, K. Kern, and M. Gironi, Giant Spin Splitting through Surface Alloying, *Phys. Rev. Lett.* **98**, 186807 (2007).
 - [6] P. Hofmann, The surfaces of bismuth: Structural and electronic properties, *Prog. Surf. Sci.* **81**, 191 (2006).
 - [7] S. Xiao, D. Wei, and X. Jin, Bi(111) Thin Film with Insulating Interior but Metallic Surfaces, *Phys. Rev. Lett.* **109**, 166805 (2012).
 - [8] K. Zhu, L. Wu, X. Gong, S. Xiao, and X. Jin, Quantum transport in the surface states of epitaxial Bi(111) thin films, *Phys. Rev. B* **94**, 121401(R) (2016).
 - [9] P. Fei, L. Xue-Jin, L. Zhao-Liang, Y. Shu-Li, and C. Dong-Min, Origin of the metallic to insulating transition of an epitaxial Bi(111) film grown on Si(111), *Chin. Phys. B* **19**, 087201 (2010).
 - [10] T. Hirahara, K. Miyamoto, I. Matsuda, T. Kadono, A. Kimura, T. Nagao, G. Bihlmayer, E. V. Chulkov, S. Qiao, K. Shimada, H.

- Namatame, M. Taniguchi, and S. Hasegawa, Direct observation of spin splitting in bismuth surface states, *Phys. Rev. B* **76**, 153305 (2007).
- [11] C. R. Ast and H. Höchst, Indication of Charge-Density-Wave Formation in Bi(111), *Phys. Rev. Lett.* **90**, 016403 (2003).
- [12] G. Bihlmayer, O. Rader, and R. Winkler, Focus on the Rashba effect, *New J. Phys.* **17**, 050202 (2015).
- [13] Z. Jiang, V. Soghomonian, and J. J. Heremans, Dynamic Nuclear Spin Polarization Induced by the Edelstein Effect at Bi(111) Surfaces, *Phys. Rev. Lett.* **125**, 106802 (2020).
- [14] T. Nagao, J. T. Sadowski, M. Saito, S. Yaginuma, Y. Fujikawa, T. Kogure, T. Ohno, Y. Hasegawa, S. Hasegawa, and T. Sakurai, Nanofilm Allotrope and Phase Transformation of Ultrathin Bi Film on Si(111)-7 × 7, *Phys. Rev. Lett.* **93**, 105501 (2004).
- [15] N. Kawakami, C.-L. Lin, M. Kawai, R. Arafune, and N. Takagi, One-dimensional edge state of Bi thin film grown on Si(111), *Appl. Phys. Lett.* **107**, 031602 (2015).
- [16] M. Rudolph and J. J. Heremans, Spin-orbit interaction and phase coherence in lithographically defined bismuth wires, *Phys. Rev. B* **83**, 205410 (2011).
- [17] M. Rudolph and J. J. Heremans, Electronic and quantum phase coherence properties of bismuth thin films, *Appl. Phys. Lett.* **100**, 241601 (2012).
- [18] F. Song, J. W. Wells, Z. Jiang, M. Saxegaard, and E. Wahlström, Low-temperature growth of bismuth thin films with (111) facet on highly oriented pyrolytic graphite, *ACS Appl. Mater. Interfaces* **7**, 8525 (2015).
- [19] N. Marcano, S. Sangiao, C. Magén, L. Morellón, M. R. Ibarra, M. Plaza, L. Pérez, and J. M. De Teresa, Role of the surface states in the magnetotransport properties of ultrathin bismuth films, *Phys. Rev. B* **82**, 125326 (2010).
- [20] M.-Y. Yao, F. Zhu, C. Q. Han, D. D. Guan, C. Liu, D. Qian, and J.-F. Jia, Topologically nontrivial bismuth(111) thin films, *Sci. Rep.* **6**, 21326 (2016).
- [21] X. Dong, Y. Li, J. Li, X. Peng, L. Qiao, D. Chen, H. Yang, X. Xiong, Q. Wang, X. Li, J. Duan, J. Han, and W. Xiao, Epitaxial growth and structural properties of Bi(110) thin films on TiSe₂ substrates, *J. Phys. Chem. C* **123**, 13637 (2019).
- [22] M. Kammler and M. Horn-von Hoegen, Low energy electron diffraction of epitaxial growth of bismuth on Si(111), *Surf. Sci.* **576**, 56 (2005).
- [23] T. Payer, C. Klein, M. Acet, V. Ney, M. Kammler, F.-J. Meyer zu Heringdorf, and M. Horn-von Hoegen, High-quality epitaxial Bi(111) films on Si(111) by isochronal annealing, *Thin Solid Films* **520**, 6905 (2012).
- [24] T. Tono, T. Hirahara, and S. Hasegawa, In situ transport measurements on ultrathin Bi(111) films using a magnetic tip: possible detection of current-induced spin polarization in the surface states, *New J. Phys.* **15**, 105018 (2013).
- [25] I. Markov, Theory and experiments in epitaxial growth, *Mater. Chem. Phys.* **9**, 93 (1983).
- [26] M. A. Herman, W. Richter, and H. Sitter, *Springer Series in Materials Science vol.62; Epitaxy, Physical Principles and Technical Implementation* (Springer, Berlin, 2004).
- [27] A. Koma, Van der Waals epitaxy for highly lattice-mismatched systems, *J. Cryst. Growth* **201-202**, 236 (1999).
- [28] A. Koma, K. Saiki, and Y. Sato, Heteroepitaxy of a two-dimensional material on a three-dimensional material, *Appl. Surf. Sci.* **41-42**, 451 (1990).
- [29] L. A. Walsh and C. L. Hinkle, Van der Waals epitaxy: 2D materials and topological insulators, *Appl. Mater. Today* **9**, 504 (2017).
- [30] M. Galbiati, N. Motta, M. De Crescenzi, and L. Camilli, Group-IV 2D materials beyond graphene on nonmetal substrates: Challenges, recent progress, and future perspectives, *Appl. Phys. Rev.* **6**, 041310 (2019).
- [31] H. J. Osten, J. Klatt, and G. Lippert, Van der Waals epitaxy of thick Sb, Ge, and Ge/Sb films on mica, *Appl. Phys. Lett.* **60**, 44 (1992).
- [32] A. J. Littlejohn, Y. Xiang, E. Rauch, T.-M. Lu, and G.-C. Wang, van der Waals epitaxy of Ge films on mica, *J. Appl. Phys.* **122**, 185305 (2017).
- [33] K. Ueno, T. Shimada, K. Saiki, and A. Koma, Heteroepitaxial growth of layered transition metal dichalcogenides on sulfur-terminated GaAs{111} surfaces, *Appl. Phys. Lett.* **56**, 327 (1990).
- [34] S. Yaginuma, T. Nagao, J. Sadowski, A. Pucci, Y. Fujikawa, and T. Sakurai, Surface pre-melting and surface flattening of Bi nanofilms on Si(111)-7 × 7, *Surf. Sci.* **547**, L877 (2003).
- [35] K. Wan, T. Guo, W. Ford, and J. Hermanson, Low-energy electron diffraction studies of Si(111)-(√3 × √3)R30°-Bi system: Observation and structural determination of two phases, *Surf. Sci.* **261**, 69 (1992).
- [36] N. Garcia, Y. H. Kao, and M. Strongin, Galvanomagnetic studies of bismuth films in the quantum-size-effect region, *Phys. Rev. B* **5**, 2029 (1972).
- [37] C. A. Hoffman, J. R. Meyer, F. J. Bartoli, A. Di Venere, X. J. Yi, C. L. Hou, H. C. Wang, J. B. Ketterson, and G. K. Wong, Semimetal-to-semiconductor transition in bismuth thin films, *Phys. Rev. B* **48**, 11431 (1993).
- [38] H. Chu and W. Zhang, Quantum size effect and electric conductivity in thin films of pure bismuth, *J. Phys. Chem. Solids* **53**, 1059 (1992).
- [39] V. B. Sandomirskii, Quantum size effect in a semimetal film, *Sov. Phys. JETP* **25**, 101 (1967).
- [40] F. Y. Yang, K. Liu, K. Hong, D. H. Reich, P. C. Searson, and C. L. Chien, Large magnetoresistance of electrodeposited single-crystal bismuth thin films, *Science* **284**, 1335 (1999).
- [41] T. Arisaka, M. Otsuka, and Y. Hasegawa, Investigation of carrier scattering process in polycrystalline bulk bismuth at 300 K, *J. Appl. Phys.* **123**, 235107 (2018).
- [42] A. S. Fedotov, V. G. Shepelevich, I. A. Svito and V. A. Sivakov, Temperature dynamics of the electronic structure in dilute Bi-Sn alloys, *Phys. Rev. B* **97**, 075204 (2018).
- [43] D. Nakamura, M. Murata, H. Yamamoto, Y. Hasegawa and T. Komine, Thermoelectric properties for single crystal bismuth nanowires using a mean free path limitation model, *J. Appl. Phys.* **110**, 053702 (2011).